



Published in final edited form as:

Ann Biomed Eng. 2019 April ; 47(4): 1023–1037. doi:10.1007/s10439-019-02211-6.

An *In-Vitro* Flow Study Using an Artificial Circle of Willis Model for Validation of an Existing One-Dimensional Numerical Model

Hongtao Yu¹, George P. Huang¹, Bryan R. Ludwig^{2,3}, and Zifeng Yang¹

¹Department of Mechanical and Materials Engineering, Wright State University, Dayton, OH 45435, USA

²Boonshoft School of Medicine, Wright State University, Dayton, OH 45435, USA

³Department of Neurology – Division of NeuroInterventional Surgery, Wright State University/ Premier Health - Clinical Neuroscience Institute, 30 E. Apple St, Dayton, OH 45409, USA

Abstract

A one-dimensional (1D) numerical model has been previously developed to investigate the hemodynamics of blood flow in the entire human vascular network. In the current work, an experimental study of water–glycerin mixture flow in a 3D-printed silicone model of an anatomically accurate, complete circle of Willis (CoW) was conducted to investigate the flow characteristics in comparison with the simulated results by the 1D numerical model. In the experiment, the transient flow and pressure waveforms were measured at 13 selected segments within the flow network for comparisons. In the 1D simulation, the initial parameters of the vessel network were obtained by a direct measurement of the tubes in the experimental setup. The results verified that the 1D numerical model is able to capture the main features of the experimental pressure and flow waveforms with good reliability. The mean flow rates measurement results agree with the predictions of the 1D model with an overall difference of less than 1%. Further experiment might be needed to validate the 1D model in capturing pressure waveforms.

Keywords

In-vitro experiment; Hemodynamics; 1D modeling; Circle of Willis; Blood flow

INTRODUCTION

The one-dimensional (1D) numerical models have been increasingly used to provide a quick understanding of the hemodynamics of blood flow in the vascular network.

^{1,3,5,6,11,16,20,26,27,34} The hemodynamics of blood flow in variations of the CoW has been investigated through 1D numerical simulations.^{1,2,10,14,17–19} The CoW was found to display different types of anatomical variations. For instance, an incomplete CoW with missing

Address correspondence to Zifeng Yang, Department of Mechanical and Materials Engineering, Wright State University, Dayton, OH 45435, USA. Zifeng.yang@wright.edu.

CONFLICT OF INTEREST

There are no conflicts of interest that could inappropriately influence this research work.

Publisher's Note Springer Nature remains neutral with regard to jurisdictional claims in published maps and institutional affiliations.

LACA_I, the flow rate in the LICA is decreased about 10%, while the flow rate in the RICA is increased about the same amount of blood. This excessive blood causes vasodilation in the anterior communicating artery to supply blood to the LACA_II.¹⁷ This flow redirection due to the variations of the CoW was also observed *in vitro*.¹⁰ Although the structure of the CoW is nonintact with missing one arterial segment, the blood perfusion for efferent arteries is almost unchanged. To accurately capture the *in vivo* flow data, applying the patient-specific arterial parameters as the initial conditions and regulating the terminal resistance can aid in reducing the difference of the mean flow rate between the 1D simulation and *in vivo* measurement.³⁵ The 1D model can also be used to study the vascular aging effects on the hemodynamics of blood flow in the CoW.^{31,33} The aging-induced variations of the flow rate waveform in the CoW were applied as the inflow boundary conditions for the 3D CFD simulation to discover the hemodynamic parameters in cerebral aneurysms.^{32,33}

To validate the 1D model, an experimental study of the hemodynamics in a rigid physical cerebrovascular model was conducted and the measurement data was compared with the simulated results obtained from a lumped parameter model by Cieslicki *et al.*⁷ It was demonstrated that the mean values of the pressure and flow rate distributions can be well predicted by the lumped parameter model as well. Validation of the 1D model toward unsteady flow has been implemented by comparing the simulated pressure and flow rate waveforms against *in vitro* and/or *in vivo* data.^{9,18,29,30} A patient-specific 1D model was reconstructed by Reymond *et al.* and able to predict the measured pressure and flow rate in specific arteries.²⁹ Discrepancies occurred in the systolic peak may be attributed to the wave reflection from the peripheral sites due to the distensibility of distal vessels and terminal resistance. Tuning the compliance for specific vessels and terminal resistance at the outflow boundary can aid in improving the simulation results.^{28,29} It was emphasized that an *in vitro* experimental study was necessary to validate the 1D model. Flow and pressure were measured in a silicone vessel network of cardiovascular arterial model and compared with the 1D simulation results.^{1,23} The results indicated that the 1D model is able to reliably capture the main features of the measured flow and pressure waveforms.²¹

Precisely predicting the flow and pressure waveforms aids in understanding the hemodynamic changes induced by cerebrovascular diseases and their effects on the global vessel network. Considering the importance of the 1D modelling of the blood flow, it is key to validate the 1D model in capturing the hemodynamics in the cerebrovascular network. Evaluating the 1D model quantitatively against *in vivo* measurements still remains a challenge since the accurate individual physiological arterial wall properties are difficult to determine. Thus, the purpose of the current research is to address this paucity of the validation study through quantifying the accuracy of our previous numerical model using *in vitro* experimental data for the same CoW configuration. The validation primarily focused on the key dynamic features of the mass flow and pressure waveforms. A closed-loop, cerebrovascular circulation, experimental model was established in the present work aiming to validate the accuracy of the previously published 1D numerical model. The description of the experimental setup and methodology of the 1D numerical model are introduced. The results target the comparisons of the flow rate and pressure waveforms at various anatomic/model locations between the 1D numerical model and the experiment.

MATERIALS AND METHODS

3D Phantom Model of the Cow

A patient-specific complete textbook-type CoW model has been created based on the 3D rotational digital subtraction angiographic (DSA) images as shown in Fig. 1. 3D rotational DSA image databases of the CoW are available through a long-term collaboration with Miami Valley Hospital of Premier Health in Dayton, Ohio. The complexity and small dimension of original image-based physiological CoW model didn't satisfy the requirements for 3D-printing, and therefore the original image-based 3D model was repaired and smoothed to a well-shaped and complete CoW model. An enlargement transition section from the original size to a closed standard tube size at each end was added to enable the connection to standard connectors. The final physical compliant silicone model of the CoW (isotropic thickness of 1.5 mm) was 3D printed using a prototype machine at Medisim Corporation as presented in Fig. 2. The compliant characteristics of the silicone model aims to potentially reflect the effects of the physiological vessel deformation on the pressure and flow rate waveforms. The silicone used in the modeling has; a refraction index of 1.41, an elongation percent of 350%, a tensile strength of 4.3 MPa, and a linear elastic Young's modulus of 1.5 MPa.

Cerebral Circulation Network Model

As the flow network shows in Fig. 2, a simplified closed loop cerebrovascular circulation network was established using: a pulsatile pump (Harvard Apparatus Pulsatile Blood Pump), an overflow reservoir, a silicone model of the CoW, bifurcation connectors, and multiple terminal flow control valves. The silicone model of the CoW was constructed of four afferent vessels including bilateral ICAs and vertebral arteries (VA), and six efferent vessels including bilateral posterior cerebral arteries (PCA), middle cerebral arteries (MCA), and anterior cerebral arteries (ACA). The dimension modifications of the four afferent and six efferent vessels of the silicone model were made in order for connecting with standard connectors and Tygon tubing, which was used to connect the CoW model to the artificial heart (pump) and overflow reservoir serving as the transitional components to complete the network, providing a. Overall, the current cerebral circulation network consists of 59 branches (8–47 are *in vivo* branches of the CoW shown in Fig. 3), as shown in Fig. 2.

Experimental Flow Conditions

The Harvard pump was set to output a periodic pulsatile flow wave with the mean flow rate of approximate 16 mL/s, which is falling into the range of the total flow rate entering the CoW of an average human.¹³ The pulsatile pump was set with the following settings to generate the inflow conditions: 60 beats per minute with a systolic to diastolic ratio of 35/65 with respect to time. Flow control valves were installed at the terminals of the tubes to control the flow rates and back pressures. The resistor was directly connected to an overflow reservoir to generate a constant distal pressure. The use of a single resistance at distal terminals, instead of considering compliance-resistance, aims to simplify the quantification of the parameters. Even though the compliance component could reduce the non-physiological wave reflection upstream, this effect was neglected to allow for simplification.

22

The working fluid was made by mixing water with glycerol at the ratio of 75/25 by weight. The density of the fluid was measured as $1050 \pm 3.5 \text{ kg m}^{-3}$. The viscosity of the fluid was $0.0026 \pm 0.0002 \text{ Pa s}$ measured by a 100 mL graduated cylinder, a smooth solid sphere (diameter less than that of the graduated cylinder), and a stopwatch. For the detailed description of the measurement of the viscosity we refer readers to Appendix 1.

Experimental Data Acquisition

The flow rate waveforms were measured using the ultrasonic flow meter (TS410 Tubing Flow Module, Transonic Systems Inc. Ithaca, NY, USA) with a flowsensor (ME 10 PXN) of 0.95 cm inner diameter (flow range: -10 to 10 L min^{-1} (standard flow), absolute uncertainty: $\pm 4\%$ of reading, ultrasound frequency: 1.8 MHz). The pressure was measured simultaneously using the micro-tip catheter pressure sensor (3.5F, SPR-524, Millar Instruments, Houston, TX, USA), with a pressure range of -6.7 to 40 kPa , with an instrument uncertainty of 0.31 kPa .

The flow meter and pressure transducer were calibrated by collecting, over a set time interval, the discharge of the steady flow using hydraulic pressure measurements, respectively. The linear regression equation of the pressure and flow rate to the voltage were examined as follows:

$$Q = 38.006V - 0.0336, \quad (R^2 = 0.9974) \quad (1)$$

$$P = 11901V - 1.0043, \quad (R^2 = 0.9974) \quad (2)$$

where Q represents the volume flow rate, V represents the voltage output, and P represents the gauge pressure value. During the experiment, the pressure and flow rate data were sampled at 1000 Hz and collected through the software LabVIEW V2011 with an in-house program to convert the voltage reading to flow rate (mL s^{-1}) and pressure (Pa), respectively. The flow signal (both pressure and flow rate) has an approximate frequency of 1 Hz , and the resonance frequency of the measurement system is beyond 1000 Hz , therefore, the measured signal is falling into the transmission band with satisfactory frequency response.

The experimental data was acquired at 13 locations, highlighted in red circles as shown in Fig. 2, including the main artery, CCA, SA, L/R ICA-I, L/R VA-I, L/R ACA-VI, L/R MCA-VII, and L/R PCA-VI. The dimensionless value of the locations is defined as: $L_{\text{entry}}/R_{\text{local}}$, where L_{entry} denotes the distance from the entry (exit of the pump) to local position, and R_{local} denotes the local radius. Thus, the corresponding dimensionless values of the 13 measurement locations are: $L_{\text{entry}}/R_{\text{local}} = 31.45, 103.77, 105.35, 183.96/183.96, 190.25/185.53, 330.50/286.48, 426.10/413.52, 406.86/402.14$. It should be noted that the measurements couldn't be obtained within the silicone model due to the limited spaces for the flowsensor and tortuous vessel features for the micro-tip catheter. Phase-averaging method was used to average the measured 150 sample waveforms of flow and pressure,

respectively. The detailed description of the phase-averaging method we refer readers to Appendix 2. Experimental uncertainty was computed by combining the random and systematic errors at the 95% confidence level, whereby $S_{\text{total}} = \sqrt{S_{\text{ran}}^2 + S_{\text{sys}}^2}$, where S_{ran} represents the random error and S_{sys} represents the systematic error.

1D NUMERICAL MODEL

The one-dimensional governing equations for blood flowing in a vessel are given by Huang *et al.* and Yu *et al.*^{16,33}:

$$\frac{\partial A}{\partial t} + \frac{\partial Q}{\partial x} = 0 \quad (3)$$

$$\frac{\partial Q}{\partial t} + \frac{\partial}{\partial x} \left(\alpha \frac{Q^2}{A} \right) + \frac{A}{\rho} \frac{\partial P}{\partial x} + \frac{f}{\rho} = 0 \quad (4)$$

where A , Q , and P represent the cross-sectional area, the volume flux, and the average internal pressure, respectively; t is time; x is the axial coordinate along the vessel; α is kinetic energy coefficient, a value of 1 is used by assuming a uniform velocity distribution in cross section. The density and viscosity were specified as the same values as used in the experiment. f is the friction force per unit length of the vessel and can be defined as, $f = 2(\gamma + 2)\mu\pi U$, where U is the velocity in the axial direction.⁴ The value of γ is determined based on the assumption of the velocity profiles, where $\gamma = 9$ represents a blunt velocity profile and $\gamma = 2$ represents a parabolic velocity profile. In the experiment, the unsteady pulsatile flow waveform employed as the inflow boundary condition would produce turbulent flows both by bi-direction cross-flows (in communicating arteries and during end diastolic period) and flow separations (at junctions), and therefore a blunt velocity profile representing turbulent flows was assumed in the 1D model. Then, the friction term can be written as $f = 22\mu\pi U$.⁴

The Eqs. (3) and (4) were closed by a wall law to relate the internal pressure to the area of the cross-section of the vessel. In the Eq. (4), the internal pressure can be expressed as:

$$P(x, t) = P_e(x, t) + K(x) \oslash (A(x, t), A_o(x, t)) + P_o \quad (5)$$

where P_e is the external pressure, $K(x)$ represents the elastic properties of the vessel wall. P_o represents the reference pressure at which $A = A_o$.

The function $\oslash(x, t)$ and $K(x)$ are assumed of the forms:

$$\varnothing(x, t) = \sqrt{\frac{A(x, t)}{A_0(x, t)}} - 1, \quad K(x) = \frac{E(x)h(x)}{(1 - \nu^2)R(x)} \quad (6)$$

where $E(x)$ represents the Young's modulus, $h(x)$ represents the thickness of the vessel wall, $R(x)$ represents the local radius, and ν represents the Poisson ratio and is equal to 0.5. The equations used to describe the vessel junctions were formulated by Riemann variables, conservations of mass, and Bernoulli equation.²⁶

The terminal resistance was computed by using lumped parameter models (0D), which adopts a single R electrical analog model. The governing equation of the 0D model can be written as $Q_{1D} = \frac{P_{1D} - P_{out}}{R_T}$, where Q_{1D} and P_{1D} are the flow rate and pressure at the outlets of the 1D model, herein, P_{out} is the constant hydraulic pressure generated by the reservoir with zero Pa as the reference pressure by calibrating the pressure transducer. R_T is the total peripheral resistance at the terminals of the 1D model, as shown in Table 1. The terminal resistances were examined from the mean pressure and flow rate measured at the in-lets and exits of the flow control valves in the experiment.

The 0D and 1D governing equations were solved using the optimal third-order total variation diminishing (TVD) Runge–Kutta method and shock-capturing TVD scheme. For the details of the numerical scheme, we refer readers to the previously published report.¹⁷ The simulation parameters used in the 1D model was directly measured from the experiment setup, such as the length, radius, and thickness of vessels, as shown in Table 2. It should be noted that the diameter defined in the 1D model was gradually changed along the vessel and expressed as a linear function of the length ratio for a vessel segment:

$$R_{local} = R_{in} + \frac{L_{local}}{L_{total}}(R_{in} - R_{out}).$$

Inflow conditions were specified with the flow rate waveform measured from the exits of the pulsatile pump. The Young's modulus of the Tygon and the silicone tubing were set as 6.7 MPa and 1.5 MPa which were measured experimentally as 6.73 ± 0.12 MPa and 1.51 ± 0.02 MPa, respectively.

RESULTS

The main 3D flow features with inlets and exits highlighted in the CoW model was presented in Fig. 3, and the label number of the vessels is corresponding to the diagram in Fig. 2. The flow pathway was highlighted using two different colors of dye (blue for right and red for left arteries), light blue and purple color were observed in the mixing region. The *in vitro* flow and pressure waveforms in the afferent and efferent vessels of the simplified, artificial, cerebral circulation model were measured and presented in Figs. 4, 5, 6, and 7. The instantaneous waveforms of pressure shown in Fig. 4 display smooth curves in periodic cardiac cycles, whereas the flow waveforms demonstrate major fluctuations around the systolic peak and end diastolic regions. This oscillation could result from the turbulent or undeveloped flow occurring in the ultrasonic field of the flowsensor. Figures 5, 6, and 7 present the phase-averaged waveforms with their experimental uncertainty and the

comparisons with the 1D numerical solutions. Overall, the pressure and flow waveform on both right and left side were almost identical since the vessel network is symmetric. Figure 8 presents the sensitivity study of the vessel compliance on the pressure and flow rate waveforms. It is observed that the compliance has a significant effect on the pressure and flow rate waveforms.

The computational results of the 1D model of the same configuration as the artificial model was evaluated by comparing the flow and pressure waveforms at thirteen selected locations within the flow network. Figure 5 and 6 depict the pressure and flow rate waveforms comparisons of the experiment with the 1D model at the center point of the upstream vessels of the CoW, including the main artery, CCA, SA, L/R ICA, and L/R VA-I. The comparison results indicate that the pressures occurring within the systolic time interval (between 0.25 and 0.6 s) can be accurately reproduced by the 1D model. However, the 1D model underestimated the pressure by roughly 15.38% in the systolic upstroke region and overestimated the pressure by about 21.72% in the diastolic runoff region. The comparisons of the flow rate waveforms show a good agreement between the 1D simulation and *in vitro* measurement. As can be seen from the flow rate comparisons in the L/R ICA-I, SA and L/R VA-I, there are oscillations at the systolic peak region observed in the numerical results. This phenomenon could result from the sudden area contraction from a large-diameter to a small-diameter of the tubing. Due to the insufficient tapering length of the connectors, a slight wave reflection to upstream was generated. As shown in Fig. 4, major oscillations were observed in instantaneous flow waveforms, but this oscillation was smoothed out by the phase averaging. Overall, the main features of the pressure and flow rate waveforms can be reliably captured by the 1D numerical model.

Figure 7 presents the pressure and flow rate comparisons of the experiment with the 1D model in 6 downstream vessels of the CoW model, including the L/R ACA, L/R MCA, and L/R PCA. It is demonstrated that the simulated pressure waveforms are capable of capturing the main characteristics obtained from the *in vitro* measurement data in the systolic region (between 0.25 and 0.69 s). Similarly, the 1D model under-predicts the pressure at the systolic upstroke (before 0.25 s) and over-predicts the pressure at the diastolic runoff (after 0.69 s) regions. The under-prediction of flow at diastolic runoff was derived from the dirotic notch produced at upstream arteries as shown in Figs. 5 and 6. However, in the experiment, the dirotic notch was attenuated leading to a relatively smooth curve, as shown in Fig. 7. The mean values of the pressure and flow rates of the simulated and *in vitro* experimental results were compared in Table 3. Good agreement is noted from the flow rate comparisons, where the overall errors between simulated and measured results are much smaller than 1%. However, significant discrepancies of pressure comparisons can be observed in the upstream arteries including the main artery, CCA, SA, L/R ICA-I, and L/R VA-I. One such example is the maximum error of 35.30% obtained from the L/R ICA-I. Thankfully, the overall errors of pressure in downstream arteries are less than 10% including; L/R ACA-VI, L/R MCA-VII, and L/R PCA-VI. These notable differences between pressure comparisons derived from the 1D model and experimental model are attributed to the mismatches that occurred at the pre-systolic and the diastolic period.

Figure 8 presents the changes in the pressure and flow rate waveforms in two selected vessels, LICA-I and LMCA-VII, induced by increasing and decreasing the entire Young's modulus of the vessels by 5 and 10 times. The Young's modulus reflects the stiffness of vessels, where higher stiffness results in increasing of the wave speed within the vessel network and the pressure pulse.³³ Pressure oscillations were observed when increasing the Young's modulus (decreased compliance), while flow oscillations were observed when reducing the Young's modulus (increased compliance). The pressure oscillations could result from the strong pressure wave reflection from the terminals.³³ Conversely, the low Young's modulus is able to decrease the wave speed, reduce the pressure peak, and weaken the strength of the pressure wave reflection. Similarly, with decrease of the Young's modulus, the increased blood volume causes a reduced peak of flow rate.

DISCUSSION

In the present research, an experimental study of flow through a silicone arterial network has been conducted to assess the accuracy of a 1D resistive boundary condition numerical approach. The comparison results of the pressure waveforms indicate that the 1D model is able to capture the main features occurred around the systolic peak region, whereas under- and overestimation can be observed at the presystolic and diastolic runoff regions, respectively. We have shown the flow rate waveforms can be measured from the upstream vessels and these same waveforms are accurately reproduced by the 1D model. However, discrepancies of the flow rate comparisons can be observed in the downstream arteries of the CoW. It should be noted that, in the experiment, the measurement results are different from the physiological ranges, for example high pressure values were observed in the CCA in Fig. 5. This is because the measurement results were completely based on the experimental conditions, such as the length, diameter, and Young's modulus of the Tygon and silicone tubes. Therefore, the *in vitro* experimental pressure and flow rate waveforms cannot accurately reflect the physiological data and fall into the physiological ranges.

Some discrepancies between the numerical and experimental flow and pressure waveforms can be observed. The simplification of the 1D reduced-order model, with the assumption of a blunt velocity profile in the friction term in Eq. (4), could contribute errors as compared to the complex flow motion in the experiment (i.e. bi-direction cross-flow and flow separations). Swirling flow patterns were observed in 3D CFD simulations of blood flow in the CoW, and the unsteady pulsatile flow rate imposed as the inflow boundary conditions gave rise to alteration of the flow direction in the communicating arteries.^{4,25} Additionally, the two types of tubes assembled in the experiment (Tygon and silicone tubes) could contribute in the discrepancies. The Tygon tube has a uniform wall thickness and elasticity, whereas these two parameters of the silicone model cannot be promised to be uniformly manufactured for the entire model, especially at junctions. The assumption of a constant elasticity and wall thickness for the silicone vessels were initialized in the 1D model probably resulting in undesirable errors. As depicted in Fig. 8, the Young's modulus can alter the pressure and flow rate waveforms significantly.

Flow control valves were adopted to connect to the overflow reservoir which served as the outflow conditions in the 1D model. This single resistance could reduce the non-

physiological wave reflection from terminals upstream in the 1D blood flow simulation.³ Matthys *et al.* evaluated the effects of different 0D models on the upstream pressure and flow rate waveforms, including resistance–inductance and resistance–compliance–resistance.²¹ The results indicated the adding of inductance can increase the oscillations in waveforms. However, the RCR model is able to reduce the oscillations and achieve a smooth curve due to Windkessel effect.²²

Even though the current 1D model is able to reproduce the *in vitro* pressure and flow waveforms, it is still challenging to predict the hemodynamics *in vivo*. First of all, the material properties of the current experimental silicone model differ from the physiological vessel wall properties. The dynamic behavior of the silicone model is linearly elastic and relatively isotropic. Conversely, the physiological vessel wall properties exhibit a nonlinear elastic dynamic behavior, where the slope of the stress–strain relationship changes with the deformation of the elastin and collagen during systole.⁸ Ghigo *et al.* stated that the dynamic response of the arterial wall also related to the blood properties, increasing the difficulty of determining accurate arterial wall properties.¹² On the other hand, the surrounding tissues can also affect the hemodynamics of blood flow by reducing the wall strain and stress to restrict the radial deformation of the arterial wall.²¹ Failing to account for the nonlinear dynamic behavior of the vessel wall due to the physiological wall properties and surrounding tissues in the 1D model could cause high pressure pulse and oscillations.^{8,28} The viscoelasticity model is able to reduce the errors between the numerical and experimental results particularly on damping peripheral oscillations by considering the vessel wall viscosity.^{1,23,24,28,36} Tuning the viscoelasticity for specific vessels and terminal resistance at the outflow boundary can aid in improving the simulation results as compared to the *in vivo* data.²⁹ Overall, the further experimental study and improvement of the numerical modeling are required to improve the comparison results through improving the uniformness of the wall thickness and elasticity of the model within the entire flow network. In the meantime, considering the effects of the viscoelasticity model in the numerical model may further improve the accuracy of the prediction of *in vivo* data.

Our greatest limitation of the current work is the unavailability of the flow characteristics in the silicone CoW model due to its limited space, such as bi-direction cross-flows occurred along the communicating arteries.⁸ A better understanding of these flow behaviors could aid in our evaluation of the shunting within the variations of the CoW and further assess the accuracy of the 1D approach. Moreover, a single resistance component adopted at the terminals of the experimental flow network could cause non-physiological reflections upstream resulting in wave oscillations. This effect was demonstrated in measured flow waveforms, but not found in pressure profiles. The influence of different terminal boundary conditions on the pressure and flow waveforms will be investigated in future studies, especially the three elements RCR boundary conditions. On the other hand, the imposed terminal resistance obtained in the experiment accounted for the total resistance of the entire vessel network. The significant curvature of the experimental vessels may increase the local resistance resulting in local flow alterations, and this effect wasn't considered in the 1D model and could be a reason to cause the discrepancies in flow comparisons. Lastly, the non-uniform manufactured wall thickness of the silicone model is an admitted limitation causing difficulties on quantifying the inner luminal dimensions to input as initial parameters for the

1D model. Consequently, significant discrepancies in flow and pressure comparisons were observed in efferent vessels. Collectively, an accurate prediction of the pressure waveforms within the compliant CoW model is difficult. Our most notable finding is the quantitative mean flow rates through all measured arteries can be precisely predicted by the 1D model.

ACKNOWLEDGMENTS

The authors would like to acknowledge the Translational Research Development Grants from the Office of Research Affairs at Wright State University.

APPENDIX 1:: THE MEASUREMENT OF THE VISCOSITY OF THE WORKING FLUID

To measure the viscosity of the working fluid, a falling sphere method was used. The relationship between the viscosity of the working fluid and the terminal velocity of the sphere can be determined as $\mu = 2gr_s^2(\rho_s - \rho_1)/9u_t$, where μ is the viscosity of the working fluid, g is acceleration due to gravity (a fixed value of 9.8 m s^{-2}), r_s is the radius of the sphere, ρ_s is the density of the sphere, ρ_1 is the density of the working fluid, and u_t is the velocity of the sphere. Briefly, in a graduated cylinder, a sphere was allowed to fall between a certain distance with marked positions at the top and bottom through the working fluid. A stopwatch was used to record the time during the sphere falling through the marked distance and its velocity was determined. The density of the sphere and working fluid was measured by dividing the mass by the volume. With having all the parameter values, the viscosity of the working fluid can be computed by the above equation.

APPENDIX 2:: PHASE-AVERAGING METHOD

The 150 measurements were split into individual waveforms by defining a reference point to distinguish each complete cardiac cycle. The reference point was chosen at the middle point of the rising edge of waveform to ensure the accuracy of the alignment of waveforms, because less fluctuation was observed in this region. The time scale for each waveform was normalized by dividing by its time interval for phase-based averaging. For pressure curves, the individual pressure waveform was end-diastolic aligned in the time domain for averaging.

REFERENCES

1. Alastruey J, Khir AW, Matthys KS, Segers P, Sherwin SJ, Verdonck PR, Parker KH, and Peiró J. Pulse wave propagation in a model human arterial network: assessment of 1-D visco-elastic simulations against in vitro measurements. *J. Biomech* 44(12):2250–2258, 2011. [PubMed: 21724188]
2. Alastruey J, Parker KH, Peiró J, Byrd SM, and Sherwin SJ. Modelling the circle of Willis to assess the effects of anatomical variations and occlusions on cerebral flows. *J. Biomech* 40(8):1794–1805, 2007. [PubMed: 17045276]
3. Alastruey J, Parker KH, Peiró J, and Sherwin SJ. Lumped parameter outflow models for 1-D blood flow simulations: effect on pulse waves and parameter estimation. *Commun. Comput. Phys* 4(2): 317–336, 2008.

4. Alastruey J, Passerini T, Formaggia L, and Peiró J. Physical determining factors of the arterial pulse waveform: theoretical analysis and calculation using the 1-D formulation. *J. Eng. Math* 77(1):19–37, 2012.
5. Blanco PJ, and Feijóo RA. A dimensionally-heterogeneous closed-loop model for the cardiovascular system and its applications. *Med. Eng. Phys* 35(5):652–667, 2013. [PubMed: 22902782]
6. Boileau E, Nithiarasu P, Blanco PJ, Müller LO, Fossan FE, Hellevik LR, Donders WP, Huberts W, Willemet M, and Alastruey J. A benchmark study of numerical schemes for one-dimensional arterial blood flow modelling. *Int. J. Numer. Method. Biomed. Eng* 31(10):e02732, 2015.
7. Cieslicki K, and Ciesla D. Investigations of flow and pressure distributions in physical model of the circle of Willis. *J. Biomech* 38(11):2302–2310, 2005. [PubMed: 16154418]
8. Danpinid A, Luo J, Vappou J, Terdtoon P, and Konofagou EE. In vivo characterization of the aortic wall stress–strain relationship. *Ultrasonics* 50(7):654–665, 2010. [PubMed: 20138640]
9. DeVault K, Gremaud PA, Novak V, Olufsen MS, Vernieres G, and Zhao P. Blood flow in the circle of Willis: modeling and calibration. *Multisc. Model. Simul* 7(2):888–909, 2008.
10. Fahy P, McCarthy P, Sultan S, Hynes N, Delassus P, and Morris L. An experimental investigation of the hemodynamic variations due to aplastic vessels within three-dimensional phantom models of the circle of Willis. *Ann. Biomed. Eng* 42(1):123–138, 2014. [PubMed: 24018609]
11. Formaggia L, Gerbeau JF, Nobile F, and Quarteroni A. On the coupling of 3D and 1D Navier–Stokes equations for flow problems in compliant vessels. *Comput. Methods Appl. Mech. Eng* 191(6–7):561–582, 2001.
12. Ghigo AR, Wang X, Armentano R, Fullana JM, and Lagrée PY. Linear and nonlinear viscoelastic arterial wall models: application on animals. *J. Biomech. Eng* 139(1):011003, 2017.
13. Grinberg L, Anor T, Cheever E, Madsen JR, and Karniadakis GE. Simulation of the human intracranial arterial tree. *Philos. Trans. A Math. Phys. Eng. Sci* 367(1896):2371–2386, 2009. [PubMed: 19414460]
14. Grinberg L, Cheever E, Anor T, Madsen JR, and Karniadakis GE. Modeling blood flow circulation in intracranial arterial networks: a comparative 3D/1D simulation study. *Ann. Biomed. Eng* 39(1):297–309, 2011. [PubMed: 20661645]
15. Hendrikse J, Raamt AF, Graaf Y, Mali WP, and Grond J. Distribution of cerebral blood flow in the circle of Willis. *Radiology* 235(1):184–189, 2005. [PubMed: 15749975]
16. Huang PG, and Muller LO. Simulation of one-dimensional blood flow in networks of human vessels using a novel TVD scheme. *Int. J. Numer. Method. Biomed. Eng* 31(5):e02701, 2015. [PubMed: 25529823]
17. Huang GP, Yu H, Yang Z, Schwieterman R, and Ludwig B. 1D simulation of blood flow characteristics in the circle of Willis using THINKS. *Comput. Methods Biomech. Biomed. Eng* 21(4):389–397, 2018.
18. Kim CS, Kiris C, Kwak D, and David T. Numerical simulation of local blood flow in the carotid and cerebral arteries under altered gravity. *J. Biomech. Eng* 128(2):194–202, 2006. [PubMed: 16524330]
19. Liang F, Fukasaku K, Liu H, and Takagi S. A computational model study of the influence of the anatomy of the circle of Willis on cerebral hyperperfusion following carotid artery surgery. *Biomed. Eng online* 10(1):84, 2011.
20. Liang F, Takagi S, Himeno R, and Liu H. Biomechanical characterization of ventricular–arterial coupling during aging: a multi-scale model study. *J. Biomech* 42(6):692–704, 2009. [PubMed: 19261285]
21. Liu Y, Dang C, Garcia M, Gregersen H, and Kassab GS. Surrounding tissues affect the passive mechanics of the vessel wall: theory and experiment. *Am. J. Physiol. Heart. Circ. Physiol* 293(6):H3290–H3300, 2007. [PubMed: 17873018]
22. Matthys KS, Alastruey J, Peiró J, Khir AW, Segers P, Verdonck PR, Parker KH, and Sherwin SJ. Pulse wave propagation in a model human arterial network: assessment of 1-D numerical simulations against in vitro measurements. *J. Biomech* 40(15):3476–3486, 2007. [PubMed: 17640653]
23. Misra JC, and Singh SI. A large deformation analysis for aortic walls under a physiological loading. *Int. J. Eng. Sci* 21(10):1193–1202, 1983.

24. Moireau P, Xiao N, Astorino M, Figueroa CA, Chapelle D, Taylor CA, and Gerbeau JF. External tissue support and fluid–structure simulation in blood flows. *Biomech. Model. Mechanobiol* 11(1–2):1–18, 2012. [PubMed: 21308393]
25. Mukherjee D, Jani ND, Narvid J, and Shadden SC. The role of circle of Willis anatomy variations in cardioembolic stroke: a patient-specific simulation based study. *Ann. Biomed. Eng* 46(8):1128–1145, 2018. [PubMed: 29691787]
26. Müller LO, and Toro EF. A global multiscale mathematical model for the human circulation with emphasis on the venous system. *Int. J. Numer. Method. Biomed. Eng* 30(7):681–725, 2014. [PubMed: 24431098]
27. Mynard JP, and Smolich JJ. One-dimensional haemodynamic modeling and wave dynamics in the entire adult circulation. *Ann. Biomed. Eng* 43(6):1443–1460, 2015. [PubMed: 25832485]
28. Raghu R, Vignon-Clementel IE, Figueroa AC, and Taylor CA. Comparative study of viscoelastic arterial wall models in nonlinear one-dimensional finite element simulations of blood flow. *J. Biomech. Eng* 133(8):081003, 2011. [PubMed: 21950896]
29. Reymond P, Bohraus Y, Perren F, Lazeyras F, and Stergiopulos N. Validation of a patient-specific one-dimensional model of the systemic arterial tree. *Am. J. Physiol. Heart Circ. Physiol* 30(3):H1173–H1182, 2011.
30. Reymond P, Merenda F, Perren F, Rufenacht D, and Stergiopulos N. Validation of a one-dimensional model of the systemic arterial tree. *Am. J. Physiol. Heart Circ. Physiol* 297(1):H208–H222, 2009. [PubMed: 19429832]
31. Xu L, Liang F, Zhao B, Wan J, and Liu H. Influence of aging-induced flow waveform variation on hemodynamics in aneurysms present at the internal carotid artery: a computational model-based study. *Comput. Biol. Med* 101:51–60, 2018. [PubMed: 30099239]
32. Yang Z, Yu H, Huang GP, Schwieterman R, and Ludwig B. Computational fluid dynamics simulation of intracranial aneurysms—comparing size and shape. *J. Coast. Life Med* 3(3):245–252, 2015.
33. Yu H, Huang GP, Yang Z, Liang F, and Ludwig B. The influence of normal and early vascular aging on hemodynamic characteristics in cardio-and cerebrovascular systems. *J. Biomech. Eng* 138(6):061002, 2016. [PubMed: 27019876]
34. Yu H, Huang GP, Yang Z, and Ludwig BR. A multiscale computational modeling for cerebral blood flow with aneurysms and/or stenoses. *Int. J. Numer. Method. Biomed. Eng* 34(10):3127, 2018.
35. Zhang H, Fujiwara N, Kobayashi M, Yamada S, Liang F, Takagi S, and Oshima M. Development of a numerical method for patient-specific cerebral circulation using 1d–0d simulation of the entire cardiovascular system with SPECT data. *Ann. Biomed. Eng* 44(8):2351–2363, 2016. [PubMed: 26721836]
36. Zhang W, Herrera C, Atluri SN, and Kassab GS. Effect of surrounding tissue on vessel fluid and solid mechanics. *J. Biomech. Eng* 126(6):760–769, 2004. [PubMed: 15796334]

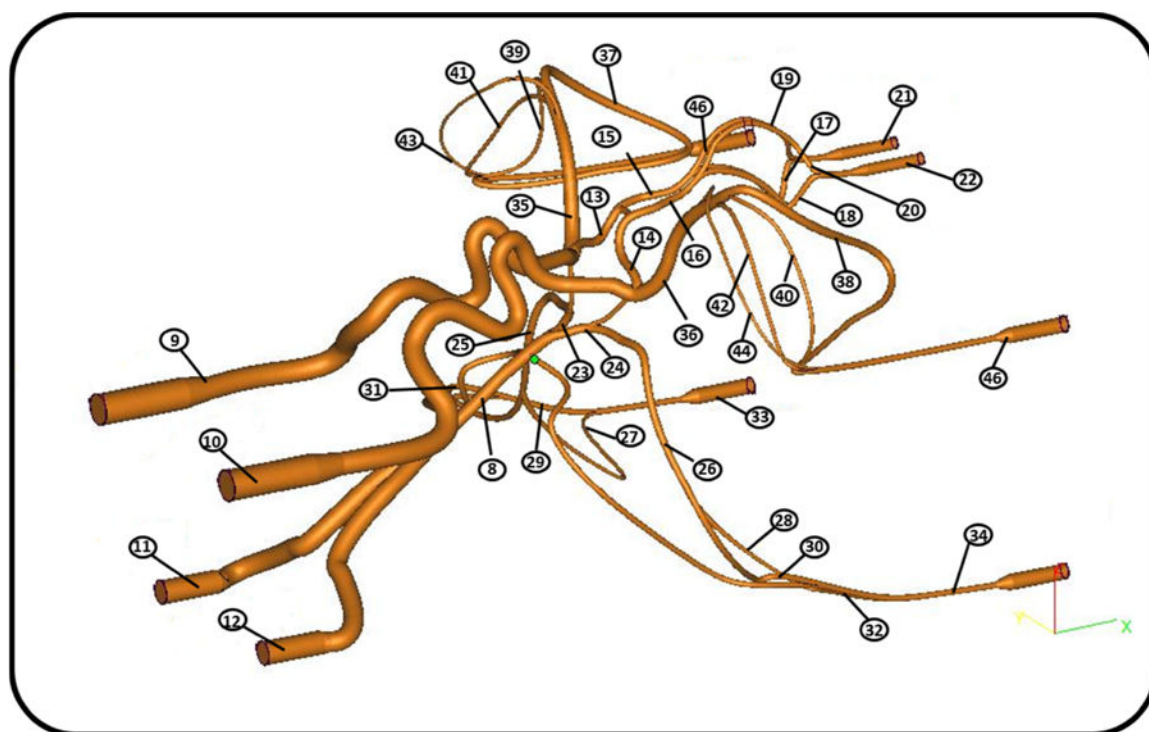


FIGURE 1.
The reconstructed CoW model from 3D angiography with standardized dimensions at inlets and outlets.

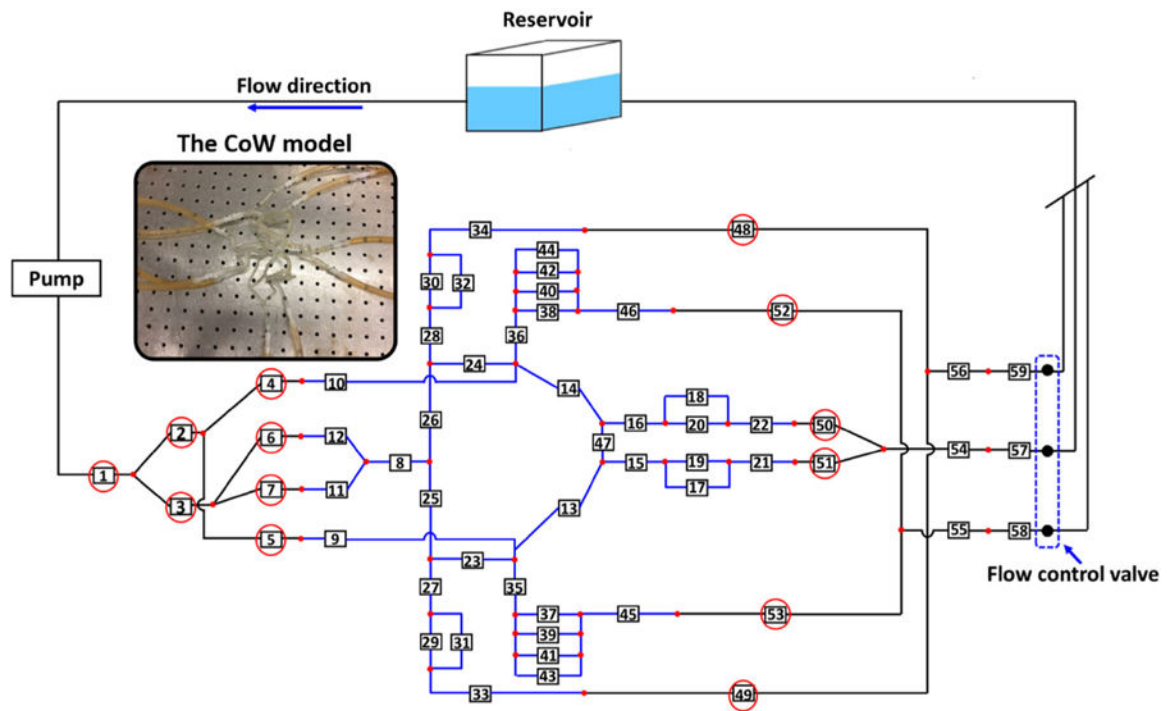


FIGURE 2.

Schematic drawing of the experimental setup. Black lines represent the Tygon tubing; Blue lines represent the silicone tubing. Vessels highlighted in red cycles are measuring locations (Color figure online).

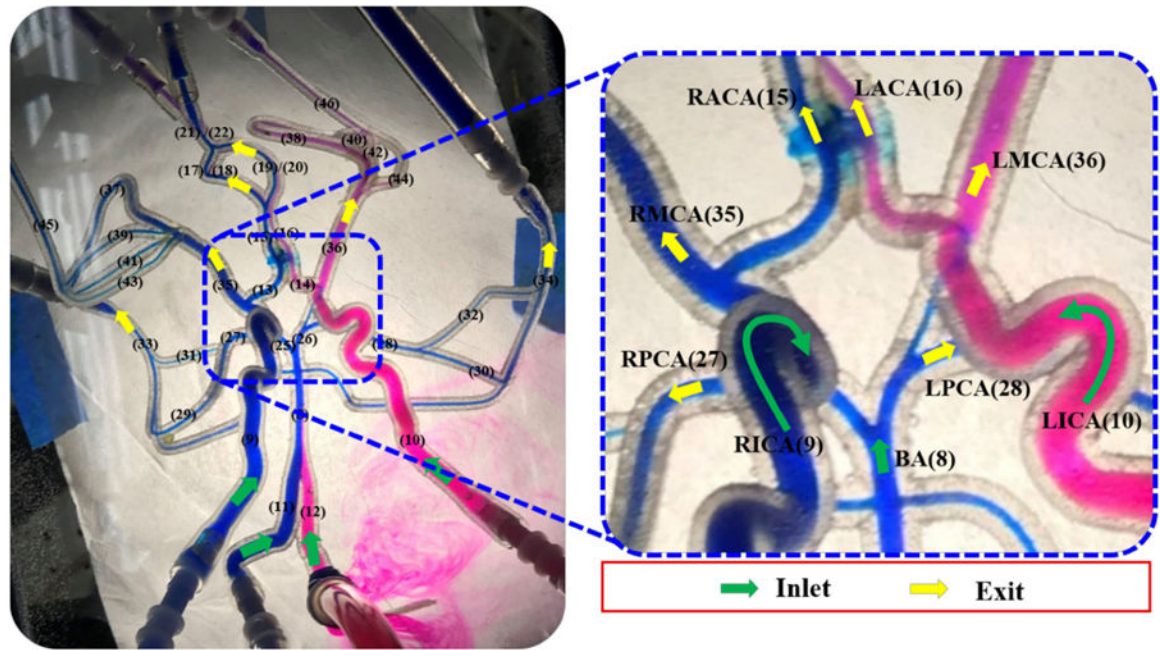


FIGURE 3.

The flow visualization in the CoW model and the closed view, the labeling of vessels is corresponding to the vessel segments in Fig. 2.

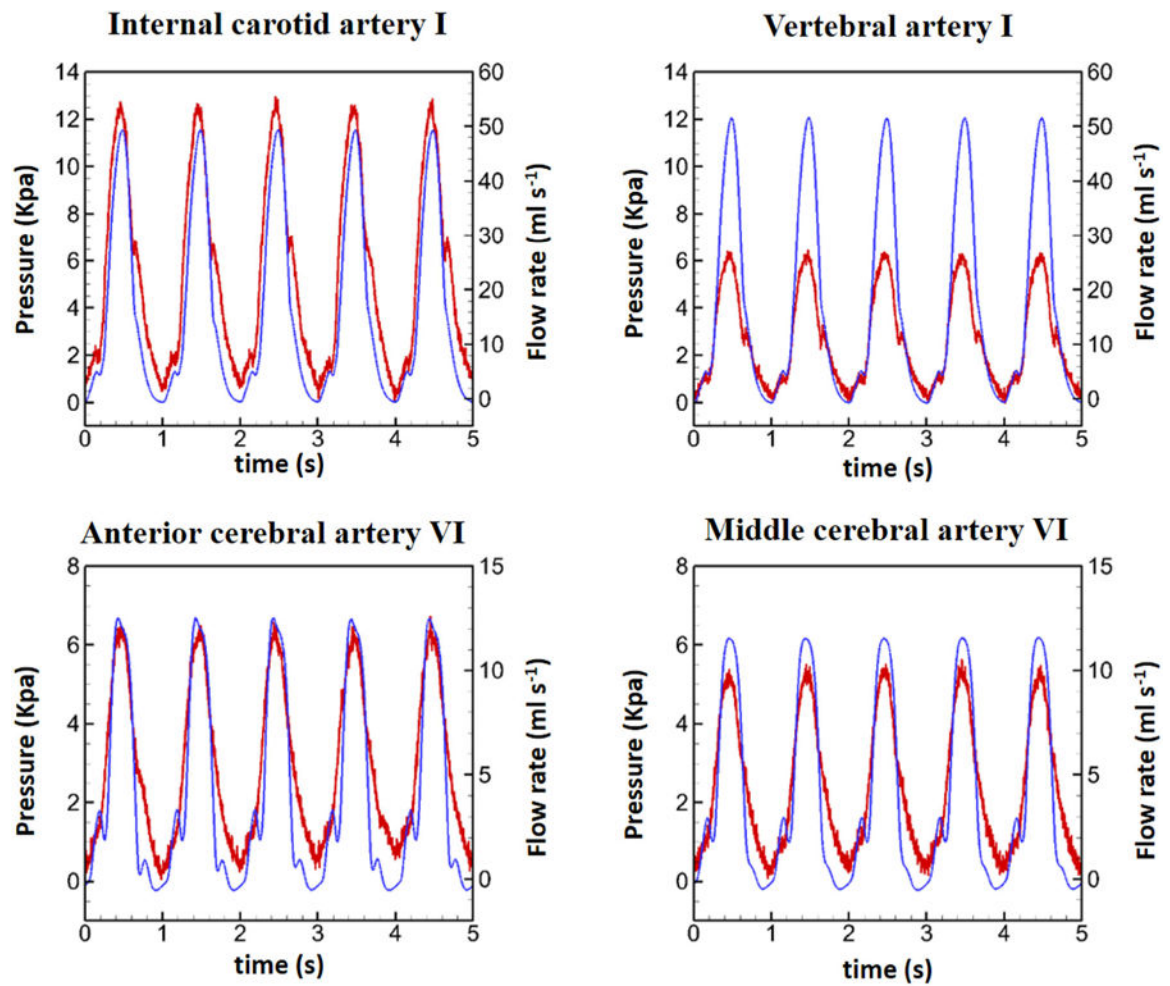
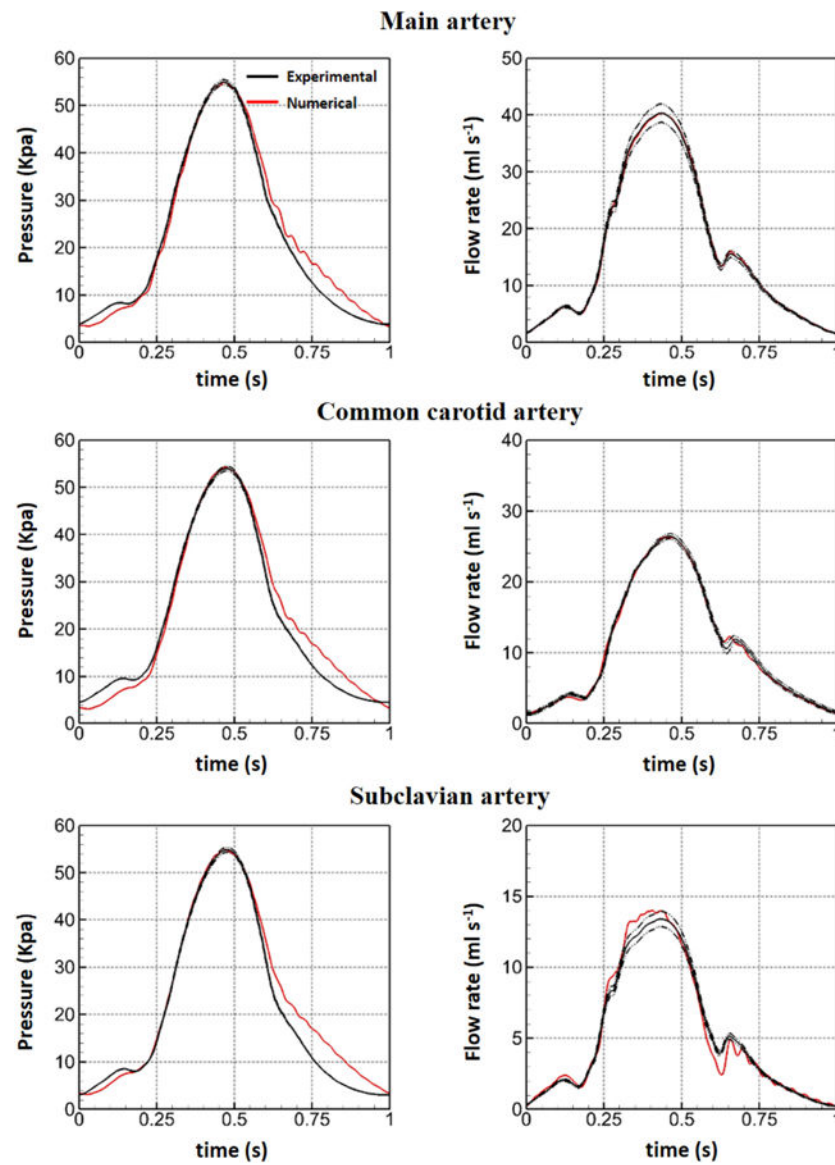


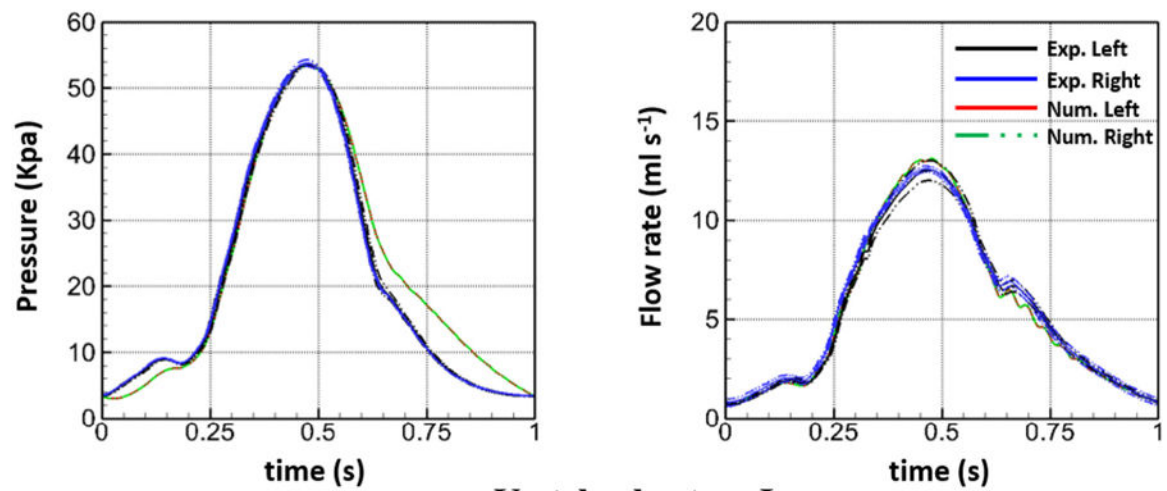
FIGURE 4.

The instantaneous pressure and flow waveforms at LICA-I, LVA-I, LACA-VI, and LMCA-VI. Blue lines represent pressure waveforms; red lines represent flow waveforms. CoW.

**FIGURE 5.**

The pressure and flow rates Comparisons of the experimental with the numerical results at main artery, common carotid artery, and subclavian artery. Black dash lines represent the total experimental uncertainty.

Internal carotid artery I



Vertebral artery I

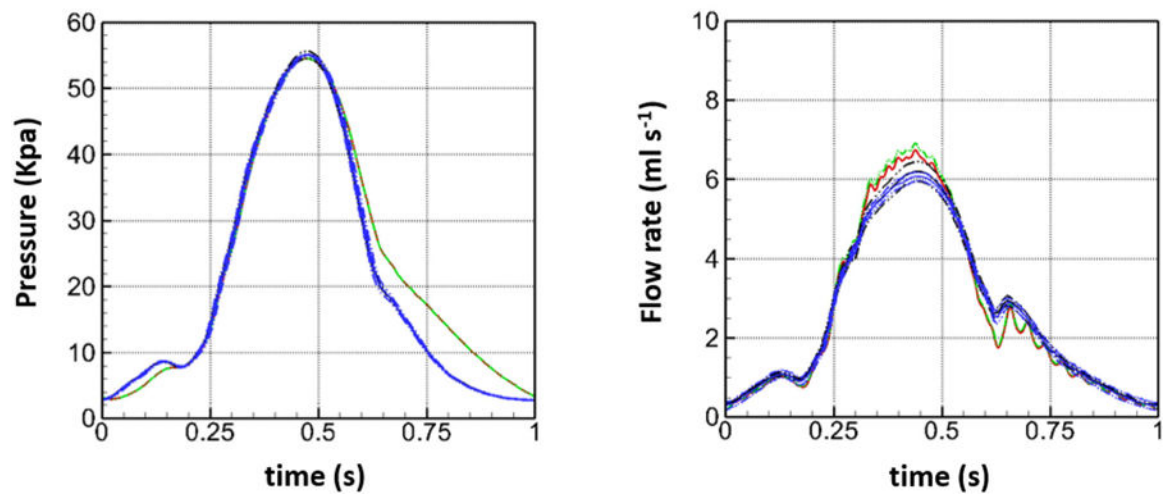


FIGURE 6.

The pressure and flow rates Comparisons of the experimental with the numerical results at R/L ICA_I and VA_I.

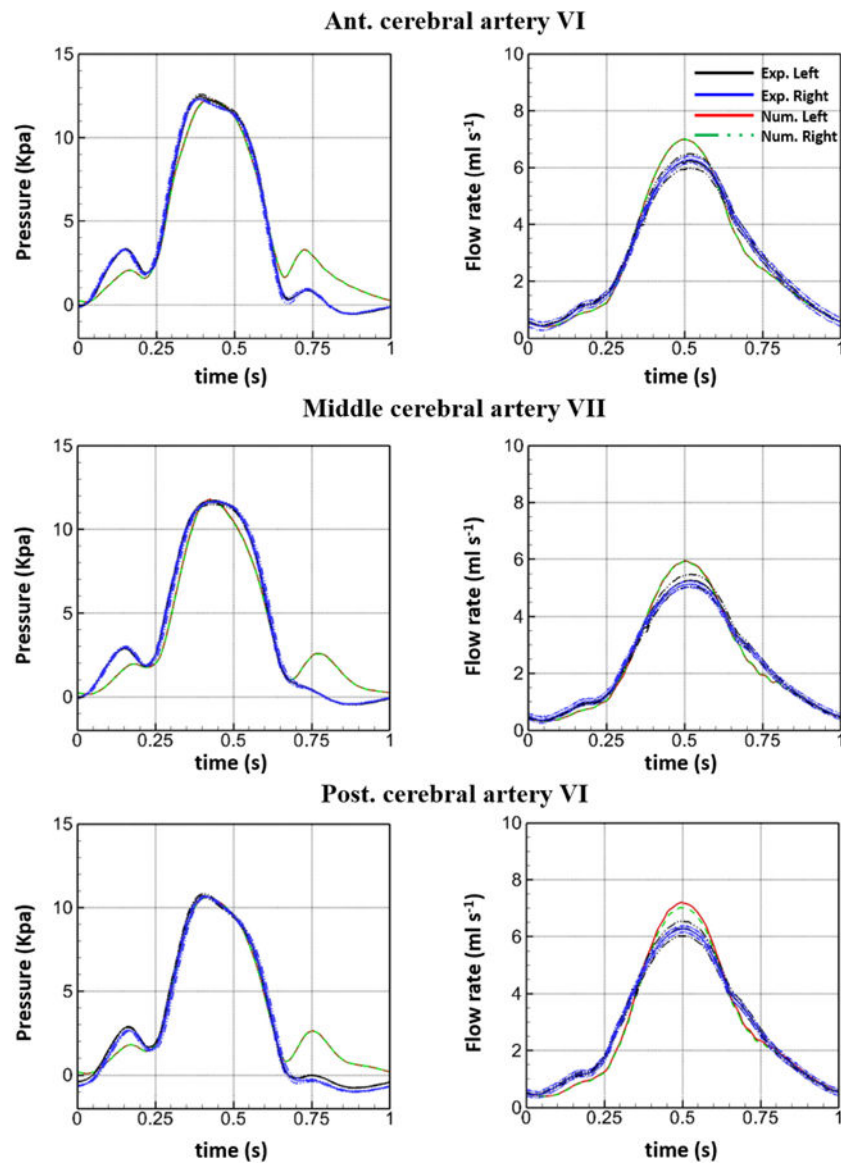
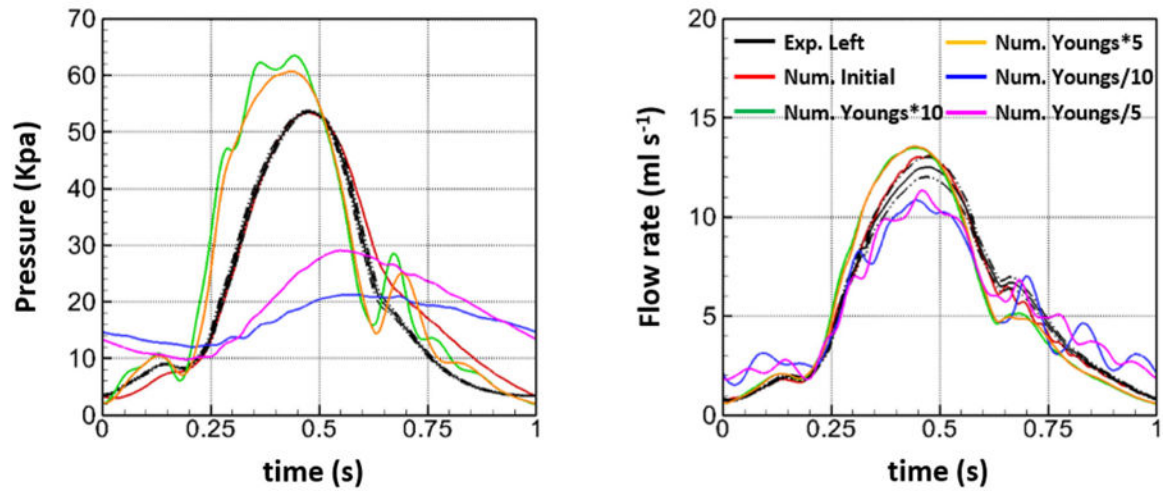


FIGURE 7.

The pressure and flow rates Comparisons of the experimental with the numerical results at R/L ACA_VI, MCA_VII, and PCA_VI.

Internal carotid artery I



Middle cerebral artery VII

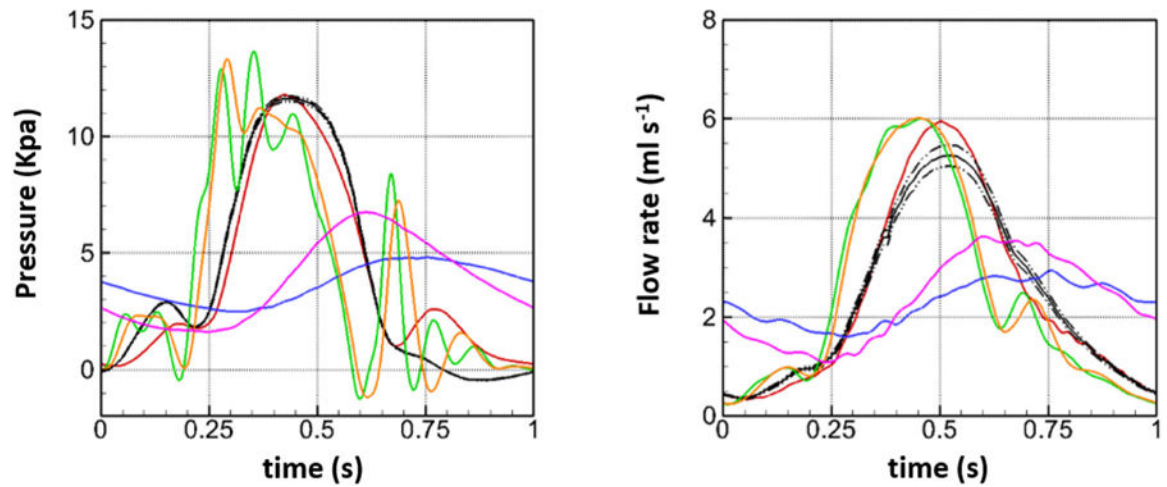


FIGURE 8.

The changes in the pressure and flow rate waveforms in two selected vessels, LICA-I and LMCA-VII, induced by increasing and decreasing the entire Young's modulus of the vessels by 5 and 10 times.

TABLE 1.

The total peripheral resistance at the terminals of the 1D model, determined from the mean pressure and flow rate measured at the inlets and exits of the flow control valves shown in Fig. 2.

Arteries	Terminal resistance (10^7 Pa s m^{-3})
Ant. cerebral a. VIII	5.06
Middle cerebral a. IX	5.00
Post. cerebral a. VIII	4.91

TABLE 2.

Parameters of the Tygon and silicone tubes presented in Fig. 2.

No.	Vessel name	Length (cm) \pm 3%	Radius _{in} (cm) \pm 5%	Radius _{out} (cm) \pm 5%	h (cm) \pm 2%
1	Main a.	20.000	0.318	0.318	0.165
2	Common carotid a.	26.000	0.318	0.318	0.165
3	Subclavian a.	27.000	0.318	0.318	0.165
4	L. int. carotid a. I	25.000	0.318	0.225	0.165
5	R. int. carotid a. I	25.000	0.318	0.225	0.165
6	L. Vertebral a. I	27.000	0.318	0.318	0.165
7	R. Vertebral a. I	26.000	0.318	0.318	0.165
8	Basilar a.	3.500	0.162	0.137	0.150
9	R. int. carotid a. II	11.500	0.225	0.155	0.150
10	L. int. carotid a. II	11.500	0.225	0.155	0.150
11	R. Vertebral a. II	4.600	0.217	0.217	0.150
12	L. Vertebral a. II	4.600	0.217	0.217	0.150
13	R. ant. cerebral a. I	1.500	0.070	0.070	0.150
14	L. ant. cerebral a. I	1.500	0.070	0.070	0.150
15	R. ant. cerebral a. II	1.600	0.065	0.065	0.150
16	L. ant. cerebral a. II	1.600	0.065	0.065	0.150
17	R. ant. cerebral a. III	2.750	0.060	0.060	0.150
18	L. ant. cerebral a. III	2.750	0.060	0.060	0.150
19	R. ant. cerebral a. IV	3.000	0.060	0.060	0.150
20	L. ant. cerebral a. IV	3.000	0.060	0.060	0.150
21	R. ant. cerebral a. V	2.500	0.065	0.115	0.150
22	L. ant. cerebral a. V	2.500	0.065	0.115	0.150
23	R. post. communicating a.	0.960	0.050	0.050	0.150
24	L. post. communicating a.	0.960	0.050	0.050	0.150
25	R. post. cerebral a. I	0.980	0.075	0.075	0.150
26	L. post. cerebral a. I	0.980	0.075	0.075	0.150
27	R. post. cerebral a. II	4.400	0.070	0.070	0.150
28	L. post. cerebral a. II	4.400	0.070	0.070	0.150

No.	Vessel name	Length (cm) \pm 3%	Radius _{in} (cm) \pm 5%	Radius _{out} (cm) \pm 5%	h (cm) \pm 2%
29	R. post. cerebral a. III	6.200	0.070	0.070	0.150
30	L. post. cerebral a. III	6.200	0.070	0.070	0.150
31	R. post. cerebral a. IV	6.000	0.070	0.070	0.150
32	L. post. cerebral a. IV	6.000	0.065	0.070	0.150
33	R. post. cerebral a. V	2.200	0.085	0.150	0.150
34	L. post. cerebral a. V	2.200	0.085	0.150	0.150
35	R. mid cerebral a. I	3.000	0.145	0.145	0.150
36	L. mid cerebral a. I	3.000	0.145	0.145	0.150
37	R. mid cerebral a. II	8.200	0.050	0.050	0.150
38	L. mid cerebral a. II	8.200	0.050	0.050	0.150
39	R. mid cerebral a. III	4.300	0.040	0.040	0.150
40	L. mid cerebral a. III	4.300	0.040	0.040	0.150
41	R. mid cerebral a. IV	3.200	0.040	0.040	0.150
42	L. mid cerebral a. IV	3.200	0.040	0.040	0.150
43	R. mid cerebral a. V	4.400	0.045	0.045	0.150
44	L. mid cerebral a. V	4.400	0.045	0.045	0.150
45	R. mid cerebral a. VI	4.300	0.065	0.150	0.150
46	L. mid cerebral a. VI	4.300	0.065	0.150	0.150
47	Ant. communicating a.	0.100	0.050	0.050	0.150
48	L. post. cerebral a. VI	67.000	0.318	0.318	0.165
49	R. post. cerebral a. VI	66.000	0.318	0.318	0.165
50	L. ant. cerebral a. VI	28.000	0.318	0.318	0.165
51	R. ant. cerebral a. VI	24.000	0.318	0.318	0.165
52	L. mid cerebral a. VII	75.000	0.318	0.318	0.165
53	R. mid cerebral a. VII	67.000	0.318	0.318	0.165
54	Ant. Cerebral a. VII	8.000	0.318	0.318	0.165
55	Mid cerebral a. VIII	8.000	0.318	0.318	0.165
56	Post. cerebral a. VII	8.000	0.318	0.318	0.165
57	Ant. Cerebral a. VIII	78.500	0.215	0.215	0.130
58	Middle cerebral a. IX	83.000	0.215	0.215	0.130
59	Post. cerebral a. VIII	61.000	0.215	0.215	0.130

r_{in} denotes the proximal radius, r_{out} the distal radius of the vessel segment, and h denotes the thickness of the vessels.

TABLE 3.

Comparisons of the mean and peak flow rate and mean pressure at various locations.

Vessels	Flow rate (mL s ⁻¹)				Gauge pressure (kPa)	
	Exp. (mean)	Sim. (mean)	Exp. (peak)	Sim. (peak)	Exp. (mean)	Sim.
Main a.	16.18 ± 0.51	16.19	40.36 ± 1.62	40.32	17.92 ± 0.37	22.76
CCA	11.00 ± 0.35	10.93	26.44 ± 0.42	26.28	16.65 ± 0.30	22.35
SA	5.22 ± 0.23	5.26	13.40 ± 0.59	13.99	17.25 ± 0.37	22.55
LICA I	5.47 ± 0.24	5.46	12.50 ± 0.50	13.11	16.33 ± 0.48	22.00
RICA I	5.47 ± 0.24	5.46	12.60 ± 0.15	13.12	16.39 ± 0.62	22.00
LVA I	2.60 ± 0.13	2.60	6.21 ± 0.25	6.74	17.08 ± 0.51	22.60
RVA I	2.60 ± 0.13	2.60	6.08 ± 0.11	6.91	17.04 ± 0.21	22.66
LACA VI	2.86 ± 0.14	2.86	6.24 ± 0.25	6.70	4.10 ± 0.15	4.39
RACA VI	2.86 ± 0.14	2.86	6.30 ± 0.13	6.70	3.98 ± 0.06	4.38
LMCA VII	2.37 ± 0.11	2.38	5.27 ± 0.21	5.94	3.91 ± 0.17	3.92
RMCA VII	2.37 ± 0.11	2.38	5.14 ± 0.12	5.94	3.96 ± 0.03	3.90
LPCA VI	2.87 ± 0.13	2.88	6.28 ± 0.25	7.20	3.24 ± 0.15	3.62
RPCA VI	2.87 ± 0.13	2.88	6.28 ± 0.12	7.03	3.15 ± 0.06	3.61